



Article

Heat Diffusion in High- C_p Nb₃Sn Composite Superconducting Wires

Emanuela Barzi ^{1,*}, Fabrizio Berritta ², Daniele Turrioni ¹ and Alexander V. Zlobin ¹

¹ Fermi National Accelerator Laboratory, Batavia, IL 60510, USA; turrioni@fnal.gov (D.T.); zlobin@fnal.gov (A.V.Z.)

² Department of Electronics and Telecommunications, Politecnico di Torino, 10129 Torino, Italy; fabrizio.berritta@studenti.polito

* Correspondence: barzi@fnal.gov

Received: 11 August 2020; Accepted: 17 September 2020; Published: 24 September 2020



Abstract: A major focus of Nb₃Sn accelerator magnets is on significantly reducing or eliminating their training. Demonstration of an approach to increase the C_p of Nb₃Sn magnets using new materials and technologies is very important both for particle accelerators and light sources. It would improve thermal stability and lead to much shorter magnet training, with substantial savings in machines' commissioning costs. Both Hypertech and Bruker-OST have attempted to introduce high- C_p elements in their wire design. This paper includes a description of these advanced wires, the finite element model of their heat diffusion properties as compared with the standard wires, and whenever available, a comparison between the minimum quench energy (MQE) calculated by the model and actual MQE measurements on wires.

Keywords: superconducting Nb₃Sn; specific heat; ceramic powders; accelerator magnets; superconducting magnet training

1. Introduction

A major focus of Nb₃Sn high field accelerator magnets for high energy physics (HEP) is on significantly reducing or eliminating their training by understanding its underlying physics mechanisms [1]. Superconducting magnets quench when their temperature increases above the current sharing temperature of the composite superconductor over a large enough volume. The temperature increase ΔT is proportional to $\Delta Q/C_p$, where ΔQ is the dissipated heat, and C_p is the volumetric heat capacity. Energy deposition that initiates quenches can emanate from a variety of sources (flux jumps, conductor motion, epoxy cracking, etc.). Other sources of magnet training are materials and material interfaces, such as insulation, impregnating material, and neighboring structural materials. All these sources contribute to a resulting “disturbance spectrum”.

Long training is a feature of any Nb₃Sn magnet. This includes both high field accelerator magnets developed and tested in the U.S. and abroad [2,3], and superconducting undulator magnets under development for installation in the advanced photon source (APS) storage ring at Argonne National Lab [4,5]. In short models of Nb₃Sn accelerator magnets, the first quench (i.e., transition from superconducting to normal phase) generally occurs at 60–70% of the short sample limits and more than 20 quenches are required to reach the magnet nominal field [6]. Training duration is expected to further increase for full-scale magnets, since the number of quenches grows with magnet length, as observed for NbTi and Nb₃Sn accelerators magnets, and in superconducting undulators.

The consistent rise of critical currents density in Nb₃Sn wires has made the problem even more challenging. Perturbations result in local thermal heating that could eventually make the superconducting wire change to the normal state. In an adiabatic model, the minimum quench energy

(MQE) is simply defined as the integration of the conductor's specific heat over the temperature margin within the superconducting state. The idea to increase the MQE by inserting high specific heat (high- C_p) elements in superconducting wires dates to 1960 [7]. In the mid-2000s, a considerable improvement in stability to pulsed disturbances was obtained for NbTi windings, when distributing large heat capacity substances on the conductor during winding [8,9]. The windings were brushed with $CeCu_6$ and $HoCu_2$ in the form of powders with 50–70 μm grain size and a volumetric content of 3 to 6%. The powders were mixed with epoxy resin and the “wet-winding” process was used. The tests were performed with both small NbTi coils made of wire and larger windings made of Rutherford-type cable. The minimum quench energies of the mixed coils were several times higher than for the clean ones. It was found that the efficiency of the wet-winding with the large heat capacity powders was greatest for temperature diffusion times much smaller than the disturbance pulse duration. Nb_3Sn is an intermetallic type II superconductor with a critical temperature T_{c0} of 18.3 K and upper critical field B_{c20} up to 30 T. For comparison, NbTi has a T_{c0} of 9.8 K and B_{c20} of 14.5 T. Demonstration of an approach to increase the C_p of Nb_3Sn magnets using new materials and technologies is very important both for particle accelerators and light sources. It would improve thermal stability and lead to much shorter magnet training, with substantial savings in machines' commissioning costs.

In standard Internal Tin Nb_3Sn composite round wires, each superconducting subelement is composed of a Sn rod surrounded by Nb, enclosed in a Cu sheath. In the Restack-Rod-Process (RRP[®]) by Bruker-OST, the Nb is itself composed of dozens of microfilaments [10]. In the Tin-in-Tube by Hypertech, the Nb is in the form of hexagonal tubes [11]. In both cases, the superconducting subelements are positioned in a normal low resistance matrix to ensure some stability with respect to flux jumps and protection in case of quenching. Once the hexagonal Nb-Sn-Cu subelements and Cu rods are stacked into a Cu can to compose a billet, the billet is then drawn down into a wire of a specific size. The composite Nb-Sn-Cu subelements become superconducting Nb_3Sn and Cu-Sn (bronze) replaces the Sn after high temperature heat treatment in inert gas. An example of a 150/169 wire cross section before heat treatment is shown in Figure 1a. The number 150 refers to the sum of superconducting elements in the wire, whereas 169 is the maximum value that could be achieved without the internal Cu hexagon. The main advantages of the Cu matrix are the high thermal conductivity and the high specific heat. The former enhances heat transfer away from the filaments, while the latter promotes the absorption of a large fraction of heat and decreases Joule heating as the superconductor loses its superconductor capability. Induced eddy currents by time-dependent fields are reduced by twisting the filaments; this solution also improves stability to flux jumps. To obtain the required current in a Rutherford cable, several strands are connected in parallel and twisted or transposed along the axial direction (Figure 1b). The strands in the Rutherford cable are not insulated from each other for letting the current redistribute in the case of localized defects or quenches [12].

Both Hypertech and Bruker-OST have attempted to introduce high- C_p elements in their wire design [13]. This paper includes a description of these advanced wires, the finite element model of their heat diffusion properties as compared with the standard wires, and whenever available, a comparison between the MQE calculated by the model and actual MQE measurements on wires.



Figure 1. (a) Cross section before heat treatment of 150/169 Nb_3Sn wire of the Restacked Rod Process[®] type [10]. (b) Cross section of 28-strand Rutherford cable [12].

2. Wire Sample Description

Examples of the two high- C_p composite wires that were modeled for thermal diffusion are shown in Figure 2. In both cases, some of the superconducting and Cu hexagons in the billet were replaced by Cu tubes containing a mixture of Cu and Gd_2O_3 ceramic powders. It is known that Gd_2O_3 has a high specific heat at low temperatures, e.g., the monoclinic structure shows a peak at 3.8 K [14]. Cu powder is added to the composite to enhance thermal diffusivity among the high- C_p particles and to soften the high- C_p element for drawing. Table 1 contains the thermal properties of the materials used in this work, including Gd_2O_3 . The Hypertech wire had 12 high- C_p subelements, six larger at the center, and six smaller at the outer corners. The Bruker-OST wire had 24 high- C_p subelements all placed on the outermost row to provide a more efficient interception of the heat flux from the wire surface. Hypertech used a Cu powder of -325 mesh and nano Gd_2O_3 powder, with a Cu: Gd_2O_3 mass ratio of 1:2. Bruker-OST experimented first within a range of Cu: Gd_2O_3 mass ratios and Cu tube thicknesses and eventually selected a Cu: Gd_2O_3 mass ratio of 4:1. After restacking and drawing, the Hypertech wire was produced in short lengths down to 0.7 mm diameter, whereas the Bruker-OST billet began to break extensively at a wire diameter of 4.1 mm. Since the MQE of the Hypertech wire had been previously tested [13,15], finite element modeling of the actual wire was used to verify the model against the data. The Bruker-OST layout was instead used to study the thermal efficiency of the high- C_p tubes when arranged in a variety of different geometrical configurations.

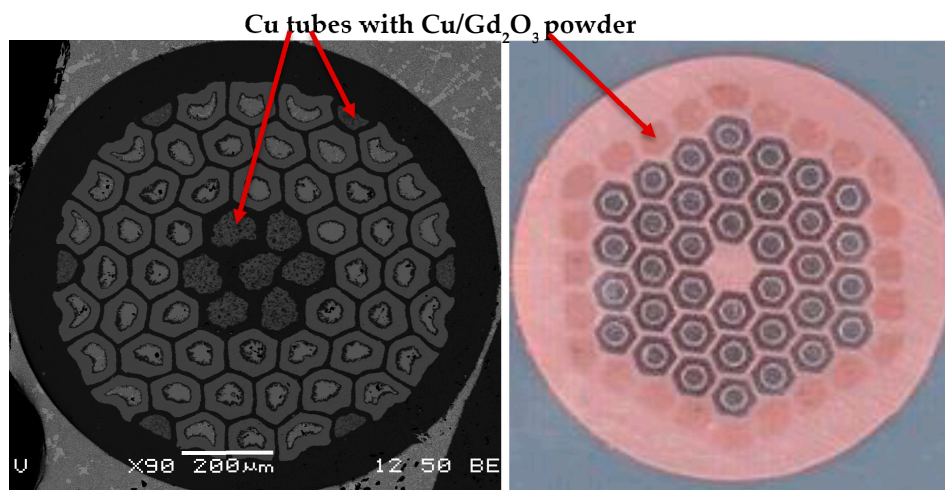


Figure 2. Left: Cross section before heat treatment of the high- C_p 48/61 Nb_3Sn wire of the Tin-in-Tube type by Hypertech [13]. Right: Cross section of the high- C_p 36/61 Nb_3Sn wire of the Restack-Rod-Process (RRP) type by Bruker-OST.

Table 1. Material properties: thermal conductivity κ (W/(m K)), specific heat C_p (J/(kg K)), thermal diffusivity a (cm^2/s) and density d [16–22].

T	Nb ₃ Sn $d = 8400 \text{ kg m}^{-3}$		Cu $d = 8960 \text{ kg m}^{-3}$		Cu-Sn (Sn wt% = 5.46) $d = 8850 \text{ kg m}^{-3}$		Stycast $d = 2400 \text{ kg m}^{-3}$		Gd ₂ O ₃ $d = 7410 \text{ kg m}^{-3}$	
	κ	C_p	κ	C_p	κ	C_p	κ	C_p	κ	C_p
4 K	174	0.41	158	0.091	1.9	0.129	0.07	0.44	6.2	22
6 K	237	0.94	237	0.226	2.9	0.194	0.11	1.70	6.2	27
8 K	308	1.85	315	0.470	3.9	0.387	0.15	3.70	6.2	29
10K	320	3.27	394	0.856	4.9	0.968	0.19	6.20	6.2	29
T	Thermal Diffusivity a [cm^2/s]									
4 K	0.505·10 ³		1.940·10 ³		16.6		0.663		0.380	
6 K	0.300·10 ³		1.170·10 ³		16.9		0.270		0.310	
8 K	0.198·10 ³		0.748·10 ³		11.4		0.169		0.289	
10 K	0.116·10 ³		0.513·10 ³		5.7		0.128		0.289	

3. Experimental Setups and Methods

3.1. Sample Heat Treatment and Critical Current Measurement

To commission an upgraded MQE measurements system several Nb₃Sn wire samples were used. In preparation to heat treatment in inert Argon, approximately 2 m long samples of Nb₃Sn composite wire are wound on grooved cylindrical Ti-alloy (Ti-6Al-4V) barrels and held in place by two removable Ti-alloy end rings. The thermal cycles are performed in three-zone controlled tube furnaces with a 12" long temperature homogeneity volume. Calibrated and ungrounded K-type thermocouples are used to monitor the accuracy and homogeneity of the reaction temperatures.

After heat treatment, the Ti-alloy end rings are removed from the Ti-alloy barrels and replaced by Cu rings. Voltage–current (V – I) characteristics are measured in boiling He at 4.2 K, in a transverse magnetic field. In standard wire critical current, or I_c , measurements, three pairs of voltage taps are used. Two pairs are placed along the center of the spiral sample 50 cm and 75 cm apart, and one pair at the Cu leads to be used for quench protection. The I_c was determined from the V – I curve using the electrical field criterion of 0.1 μ V/cm. Typical I_c measurement uncertainties are within $\pm 1\%$ at 4.2 K and 12 T. The measured I_c value is important when performing the MQE measurement at various normalized transport current ratios I/I_c .

3.2. Minimum Quench Energy (MQE) Measurement and Reproducibility

To measure the MQE, strain gauges are used as heaters. Strain gauges WK-09-125BT-350 from Micro-Measurements were glued to the samples using Stycast, with the gauge patterns (~ 4 mm in length and ~ 1.5 mm in width) centered on the wire sample and their long sides parallel to the wire axis. After curing of the Stycast, the instrumentation wires are soldered before sample and strain gauge get brushed with a thick layer (~ 1 mm) of Stycast. A 200 W KEPCO power supply provides the excitation voltage to the strain gauge. Using a LabView DAQ program, a μ s-long pulse output is generated from the power supply and the voltage across the strain gauge is measured. With the I_c of the sample first measured, a constant bias current below I_c is applied to the sample and heat pulses are fired using the strain gauge. In this study, the duration of the heat pulses was fixed at 200 μ s. A separate quench protection monitored the voltage across the sample and shut down the power supply if the quench threshold was reached. By gradually increasing the pulse power (in steps of 0.03 μ J when approaching the critical energy), the critical energy that induced a quench is defined as the MQE of the sample. The measurement error is given by the difference between the MQE achieved value and the energy provided to the heater at the previous step.

For reproducibility, the most important factor is good thermal contact between the heater and the sample. It takes some practice to develop a reliable procedure in attaching the strain gauge to the wire. Eventually, a very good reproducibility was achieved, as can be seen from Figure 3, which shows the measured MQE for a few wires as a function of the normalized transport current I/I_c . Measurement errors as described above are shown in Figure. The 108/127 RRP wire in the plot is the standard wire used in the LHC Accelerator R&D Program (LARP), which is currently in its production phase as US HL-LHC Accelerator Upgrade Project (AUP). In addition, two samples of the same 60/61 RRP wire were flat rolled before reaction from 0.7 mm to 0.56 mm (i.e., 20% deformation) to allow for a better mounting of the strain gauge.

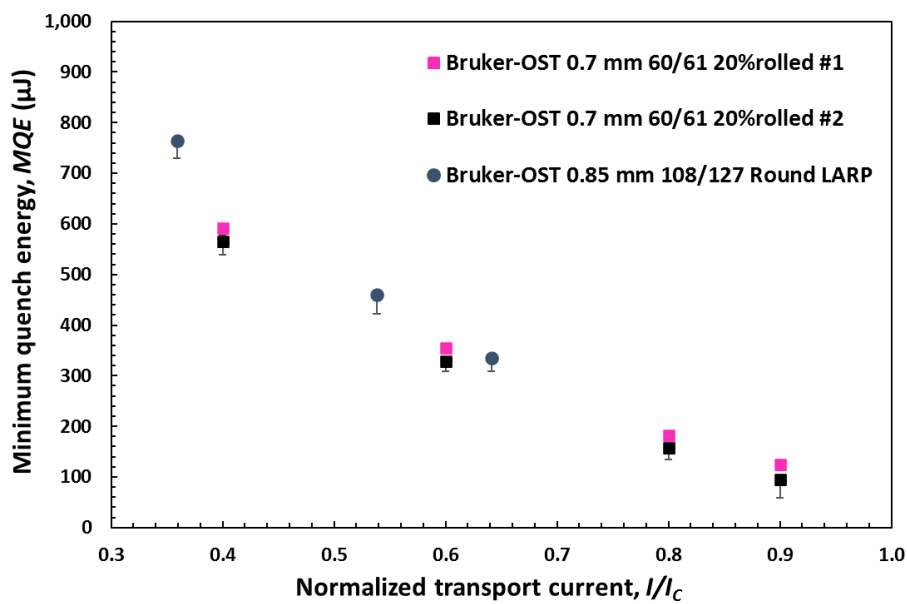


Figure 3. Minimum quench energy (MQE) as measured for a number of wires as function of the normalized transport current I/I_c .

4. Finite Element Model

4.1. Quench Origin Mechanisms

Critical current, temperature and magnetic field define a critical surface within which the superconducting state is sustained, i.e., non measurable resistivity and perfect diamagnetism. In general, a magnet operates below the critical surface, but as soon as the current is being ramped up one gets closer to the critical surface. Crossing it means that a small volume V switches to the normal resistive state. Power is therefore dissipated by Joule effect, leading to a temperature increase in the surrounding volume dV . If the temperature reached by dV approaches the critical temperature, then further power is dissipated, and the process keeps going by thermal diffusion. The normal zone propagates through the entire coil and the magnet quenches.

Two different quench mechanisms are defined: conductor-limited and energy-deposited quenches [23]. To distinguish between them, a conductor of known critical current $I_c(T,B)$ is assumed. The maximum magnetic field seen by the conductor is a function of the current itself $B = f(I)$, resulting in the following implicit equation for the maximum current I_{max} :

$$I(T_0) = I_c(T_0, f(I)) \tag{1}$$

If the quench occurs at I_{max} , then it is due to the intrinsic properties of the conductor: it is a conductor limited quench. The other type of quench occurs at a current I lower than $I_{max}(T_0)$, once that the temperature raises to $T_0 + \Delta T$ in a volume dV of the coil, such that

$$I(T_0 + \Delta T) \geq I_c(T_0, f(I)) \tag{2}$$

These quenches are energy-deposited since they take place because of an energy deposit. Hence, in conductor-limited quenches the critical surface is crossed because of a current increase, whereas in the energy-deposited quenches the critical surface is crossed due to a local temperature increase. In the following, we will consider only the latter since they are the cause of magnet training. Furthermore, the magnetic field B will be assumed to be just the external field provided by the solenoidal experimental setup.

The model is two-dimensional because it did not aim to simulate the exact absolute MQE values of each wire, but only to predict the correct MQE ratio between wires with and without high- C_p subelements. The model therefore does not take into account axial heat conduction in either wire. However, from the diffusivity values shown in Table 1, a simple calculation shows that there is very little difference in axial heat transfer between wires with and without high- C_p subelements.

Based on the concept of the minimum propagation zone (MPZ), an energy deposited quench occurs only if the local increase in temperature grows beyond a given volume V_0 inside the wire. This condition was met since the strain gauge was ~ 4 mm long and in the two-dimensional ANSYS [24] model, a unitary axial length of 1 m is assumed for both wire and strain gauge. This length is much larger than the MPZ of Nb_3Sn multifilamentary wires [16].

4.2. Materials' Properties

The Finite Element Model (FEM) of heat diffusion in Nb_3Sn wires was made using ANSYS Mechanical APDL[®]. With material properties dependent on temperature, the ANSYS model is non-linear, and iterative algorithms are required to obtain a solution with the desired accuracy [24]. Standard and high- C_p wires by Hypertech and Bruker-OST were modeled in two-dimensions as depicted in Figure 4. The coordinate system is assumed to be centered at the wire center, for each wire model. Half of the wire geometry was modeled because of symmetry with respect to the y direction. The normal wire is surrounded by the Stycast, which acts as a thermal insulator, whereas the Nb_3Sn subelements are embedded in a Cu matrix. The wire is not at the center of the Stycast to better represent the experimental setup. Since the wires are modeled after undergoing the thermal cycle, the Nb_3Sn hexagons contain Cu-Sn, rather than Sn.

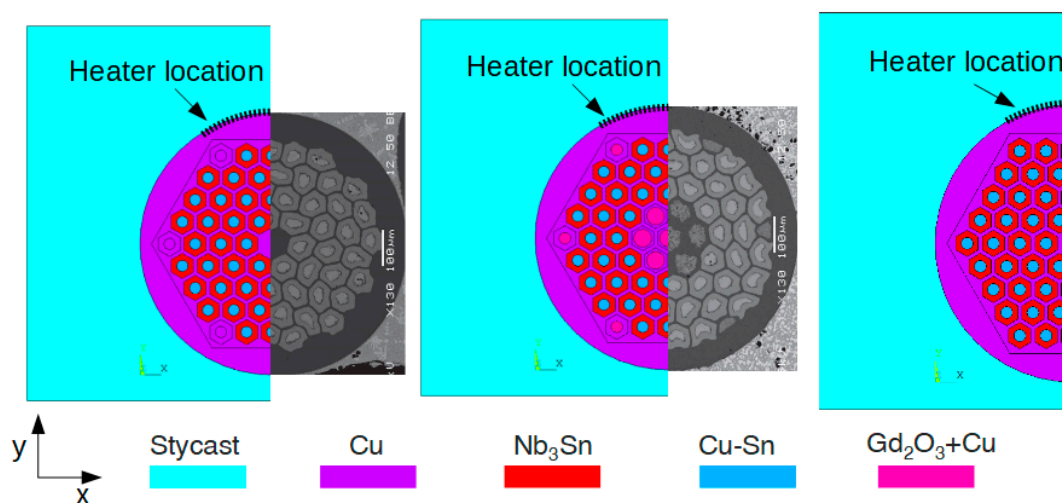


Figure 4. Left: Geometrical model used for standard 54/61 wire by Hypertech, compared with a cross section of the latter. Center: Geometrical model used for high- C_p 48/61 wire by Hypertech, compared with a cross section of the latter. Right: Geometrical model used for standard 60/61 wire by Bruker-OST.

The chosen material properties as a function of temperature are detailed in Table 1. The Nb_3Sn properties in the Table refer to the superconducting state. The effect of the applied magnetic field, $B = 12$ T, is considered only for the Cu thermal conductivity and for the Gd_2O_3 specific heat, as shown in Figure 5. All the Gd_2O_3 properties have been mixed with those of Cu to consider the powder mixture. The standard linear rule of mixtures was used, with a Cu to Gd_2O_3 ratio of 1:2. It is interesting to notice in Figure 5 that the peaking behavior of the specific heat is lost as magnetic fields are applied [17]. Nonetheless, the specific heat of Gd_2O_3 remains sufficiently high as experimental results show.

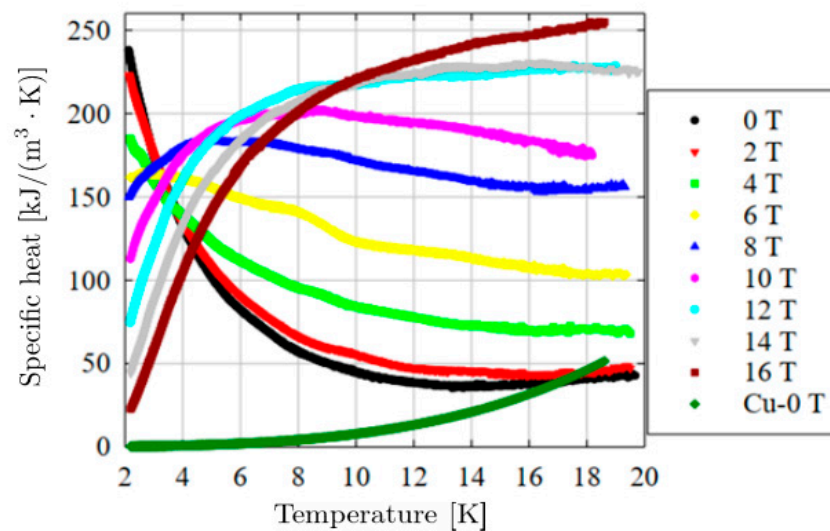


Figure 5. Measured specific heat of Gd_2O_3 [19].

4.3. Wire Geometries

As mentioned in Section 2, Hypertech and Bruker-OST standard and high- C_p wires were modeled. The FEM model was first checked against measurements of the modeled Hypertech wires. Once the model's prediction capability was verified, it was applied to several different high- C_p subelement layouts in the Bruker-OST wire.

4.3.1. Hypertech Wires

For the standard and high- C_p wires by Hypertech in Figure 4, left and center, the following geometrical parameters were used:

- Wire diameter = 0.7 mm
- Cu-Sn rods radius = Gd_2O_3 corner subelement radius = 15 μm
- Maximum superconducting subelement width = $2 \times 29/\sqrt{3}$ μm
- Thickness between two sub-elements = 10 μm
- Stycast total width W_{sty} and height H_{sty} are 1.3 mm and 1.0 mm, respectively. Stycast center was displaced along y by $(H_{sty} - R_{wire})/8$
- Gd_2O_3 central subelement radius = 23 μm

4.3.2. Bruker-OST Wires

For the standard wire by Bruker-OST in Figure 4, right, the same geometrical parameters as above were used. In this case, all the high- C_p sub-elements have the same area as the Cu-Sn rods. In addition to the standard wire, six additional geometries were simulated:

- six high- C_p sub-elements in the innermost row
- six high- C_p sub-elements at the six outermost corners
- 24 high- C_p sub-elements in the outermost row
- 24 high- C_p sub-elements in the first two innermost rows and six outermost corners
- 18 high- C_p sub-elements in the first two innermost rows
- 20 high- C_p sub-elements randomly positioned

4.4. Thermal Analysis

The next step was the choice of the thermal load to simulate an MQE experiment. In [15] a flat strain gauge was applied on top of the wire and the energy was obtained by integrating over time the dissipated power due to Joule heating in the gauge. In the two-dimensional FEM model, a thermal flux impinging on a circumference arc was chosen, corresponding to an angle $\theta \in (90^\circ, 120^\circ)$. Since we are working with half of the wire geometry, this means that the heat flux was applied to $30^\circ \times 2/360^\circ = 1/6$ of the wire circumference. It will be shown that the choice of θ changes the results by small percentages. As a boundary condition, the initial temperature is set to be $T_0 = 4.2$ K because of the He bath, whereas at the boundaries $T_{env} = 4.2$ K is kept fixed during the transient. Along $x = 0$ no boundary conditions have been applied, resulting in an adiabatic setting for ANSYS. No heat flux occurs along that line because of the symmetry. The chosen element type was PLANE55, and the mesh was sufficiently refined until no changes occurred in the second decimal digit of the wire's maximum temperature after the heat pulse.

The heat flux pulse duration was set to 200 μ s and its amplitude was evaluated by dividing the input energy by two, by the pulse duration and by the area. The factor of two derives from modeling half of the wire, whereas the area is just the arc length upon which the flux is applied multiplied by a unitary length, which is the thickness dimension used by ANSYS in two-dimensional models [24]. The goal of the model is to obtain the MQE as a function of the normalized transport current I/I_c . However, whereas in the experimental setup the current is the input and the MQE is then measured at that specific current, in this FEM model their roles are exchanged. In the FEM simulation no currents are available, just the maximum temperature of the wire is. The concept used was to consider the maximum temperature, at a given input energy, as the critical temperature associated with the required critical current. An empirical relationship for the $I_c(B, T)$ of Nb₃Sn was used [25] with the fitting parameters $I_{ref}(\epsilon) = 489$ A, $T_{c0}(\epsilon) = 16.96$ K and $B_{c20}(\epsilon) = 27.89$ T, leaving the strain undetermined. With this method, the critical current $I_{c0} = I_c(12T, 4.2$ K) was obtained, as well as the current ratio $\tilde{I}_{Tc} = I_c(12T, T_c)/I_{c0}$ of the wire at the critical current T_c for each heat flux pulse. For Nb₃Sn at 12 T, critical temperatures of 6.3 K and 4.4 K corresponded to critical current ratios of 0.2 and 0.8, respectively.

4.5. Sensitivity Analysis

To study the sensitivity of the model with respect to the chosen material properties, the FEM was tested several times, by changing the specific heat or thermal conductivity of each material separately. Each material property was varied by $\pm 20\%$. The results are summarized in Tables 2 and 3. In the Tables, "Dev." stands for "Deviation". The minimum and maximum percentage change of \tilde{I}_{Tc} ($\alpha_i = \pm 20\%$), where $\alpha_i = \pm 20\%$ represents a material property change at all temperatures, are indicated next to the associated input MQE values. It resulted that for each material property change, the minimum absolute \tilde{I}_{Tc} deviation from the original simulation occurs at the lowest MQE input value, and the maximum absolute \tilde{I}_{Tc} deviation at the maximum MQE input value. It is interesting to note that variations in the Nb₃Sn specific heat have the greatest impact on the standard wire final temperature, whereas for high- C_p wires it is the Gd₂O₃ specific heat that has the greatest impact.

Similarly, the FEM was tested also when changing the angle θ representing the extension of the thermal load around the wire. As detailed in Table 4, the angle was changed by up to $\pm 20^\circ$, and the \tilde{I}_{Tc} changes by less than 5%. Smaller angles result in lower current ratio values. This behavior can be explained with a reduced heat transfer surface at small angles, resulting in lower heat transfer towards the Stycast and therefore in a slightly higher increase in the wire temperature.

Table 2. Materials' properties sensitivity in thermal simulation of standard wire.

Thermal Conductivity Variation	Nb ₃ Sn		Cu		Cu-Sn		Stycast	
	-20%	+20%	-20%	+20%	-20%	+20%	-20%	+20%
\tilde{I}_{Tc} dev. at 320 μ J MQE (%)	-0.1	0.1	-0.2	0.1	<0.1	<0.1	-1.4	1.2
\tilde{I}_{Tc} dev. at 2300 mJ MQE (%)	-0.3	0.2	-0.6	0.5	<0.1	<0.1	-3.5	3.3
Specific Heat Variation	Nb ₃ Sn		Cu		Cu-Sn		Stycast	
	-20%	+20%	-20%	+20%	-20%	+20%	-20%	+20%
\tilde{I}_{Tc} dev. at 320 μ J MQE (%)	-3.7	3.3	-1.7	1.6	-0.3	0.3	-1.1	1.0
\tilde{I}_{Tc} dev. at 2300 mJ MQE (%)	-9.7	9.3	-4.9	4.8	-0.8	0.8	-3.0	2.8

Table 3. Materials' properties sensitivity in thermal simulation of high- C_p wire.

Thermal Conductivity Variation	Nb ₃ Sn		Cu		Cu-Sn		Stycast		Gd ₂ O ₃	
	-20%	+20%	-20%	+20%	-20%	+20%	-20%	+20%	-20%	+20%
\tilde{I}_{Tc} dev. at 860 μ J MQE (%)	-0.2	0.1	-0.4	0.3	<0.1	<0.1	-0.5	0.5	<0.1	<0.1
\tilde{I}_{Tc} dev. at 5200 mJ MQE (%)	-0.6	0.5	-1.5	1.1	<0.1	<0.1	-2.0	1.9	<0.1	<0.1
Specific Heat Variation	Nb ₃ Sn		Cu		Cu-Sn		Stycast		Gd ₂ O ₃	
	-20%	+20%	-20%	+20%	-20%	+20%	-20%	+20%	-20%	+20%
\tilde{I}_{Tc} dev. at 860 μ J MQE (%)	-1.4	1.3	-0.7	0.7	-0.1	0.1	-0.5	0.4	-5.6	4.8
\tilde{I}_{Tc} dev. at 5200 mJ MQE (%)	-5.5	5.3	-3.1	3.1	-0.4	0.4	-1.8	1.7	-13	14

Table 4. Load angle sensitivity for thermal simulation. The angle refers to the Finite Element Model (FEM) model, i.e., θ is between 0° and 180°. The original angle in simulations is 30°.

Load Angle Variation	$\Delta\theta = -20^\circ$	$\Delta\theta = -10^\circ$	$\Delta\theta = +10^\circ$	$\Delta\theta = +20^\circ$
Standard Wire				
\tilde{I}_{Tc} dev. at 320 μ J MQE (%)	-0.5	-0.1	0.1	0.3
\tilde{I}_{Tc} dev. at 2300 mJ MQE (%)	-2.0	-0.6	0.6	1.1
High-C_p Wire				
\tilde{I}_{Tc} dev. at 860 μ J MQE (%)	-1.3	-0.5	0.4	0.7
\tilde{I}_{Tc} dev. at 5200 mJ MQE (%)	-4.6	-1.8	1.4	2.5

5. Results and Discussion

5.1. Model

The results of the Hypertech wires' simulation are presented in Figure 6, where they are compared with experimental data [15]. It can be appreciated that the model is conservative with respect to the experiment. However, it correctly predicts the MQE ratio between the high- C_p wire and the standard one. This ratio is about three for both model and data. Therefore, the thermal model reproduces well the relative thermal efficiency of the high- C_p wire when compared to the standard one. Nonetheless, the MQE curves from the model are lower than the acquired data. There are differences between the experiment and model in the way that the heat is applied to the sample. In the experiment, heat is applied along 4 mm length of wire by the 4 mm long strain gauge, and conduction occurs in all directions. In the two-dimensional ANSYS model, a unitary axial length of 1 m is assumed for both

wire and strain gauge, the heat flux was directed towards the wire itself and there was no axial heat propagation. Therefore, the heat required in the simulation to reach the critical temperature is lower than in the experiment.

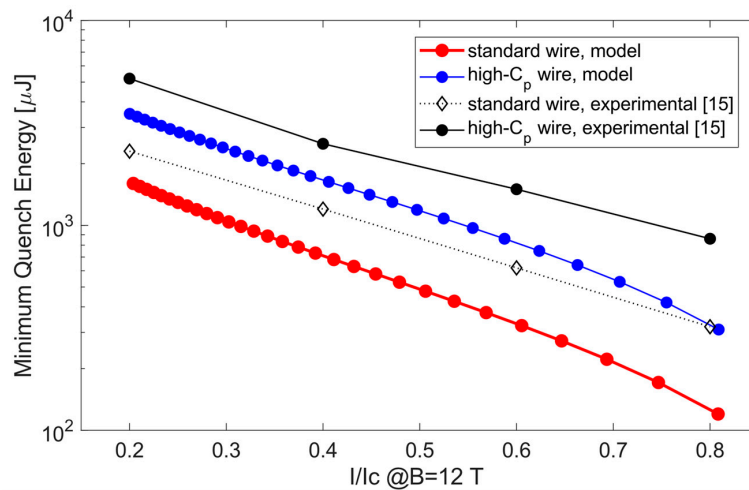


Figure 6. Comparison between MQE simulations and experimental data [15] for Hypertech wires.

Once the model’s relative prediction capability was verified, it was applied to a number of different high- C_p subelement layouts in the Bruker-OST wire. The results of the MQE simulations for the various Bruker-OST wire geometries are presented in Figure 7. It is important to outline that two pairs of curves having the same number of high- C_p subelements overlap each other. The first overlapping is for a total number of six high- C_p subelements, and the other occurs in the case of 24 total high- C_p subelements. Hence, these FEM simulations have shown that the quantity of these high- C_p components has a much greater impact on their desired thermal effect than their location. The curves having the high- C_p components far from the wire center are slightly more efficient. Nonetheless, it appears that the mechanical feasibility of high- C_p composite wires decreases the further away from the billet center these brittle tubes are inserted in the billet. Thus, the simulations have shown that it is possible to develop new structures without worrying about thermal efficiency if the number of high- C_p subelements is sufficiently high.

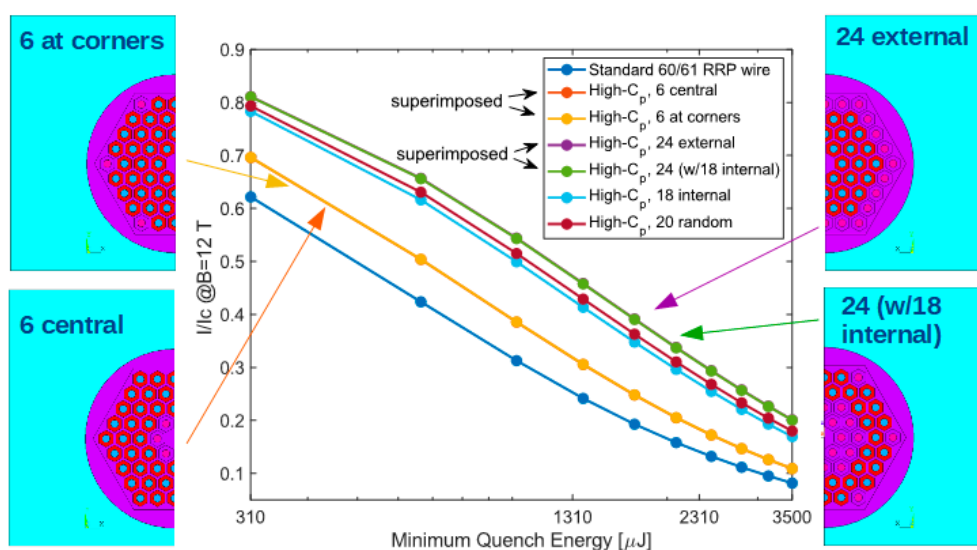


Figure 7. Thermal simulation of Bruker geometry with different high- C_p subelements location and quantity.

5.2. Experiment

To verify the model against additional experimental data, a 0.85 mm Bruker-OST LARP standard wire was wrapped with a 10 mm wide and 64 μm thick Cu/Gd₂O₃ tape before heat treatment. MQE results, measured and simulated, are shown in Figure 8 as a function of normalized transport current for the LARP-type wire bare and wrapped with the tapes. Results are comparable with the MQE achieved for the high- C_p Hypertech wire.

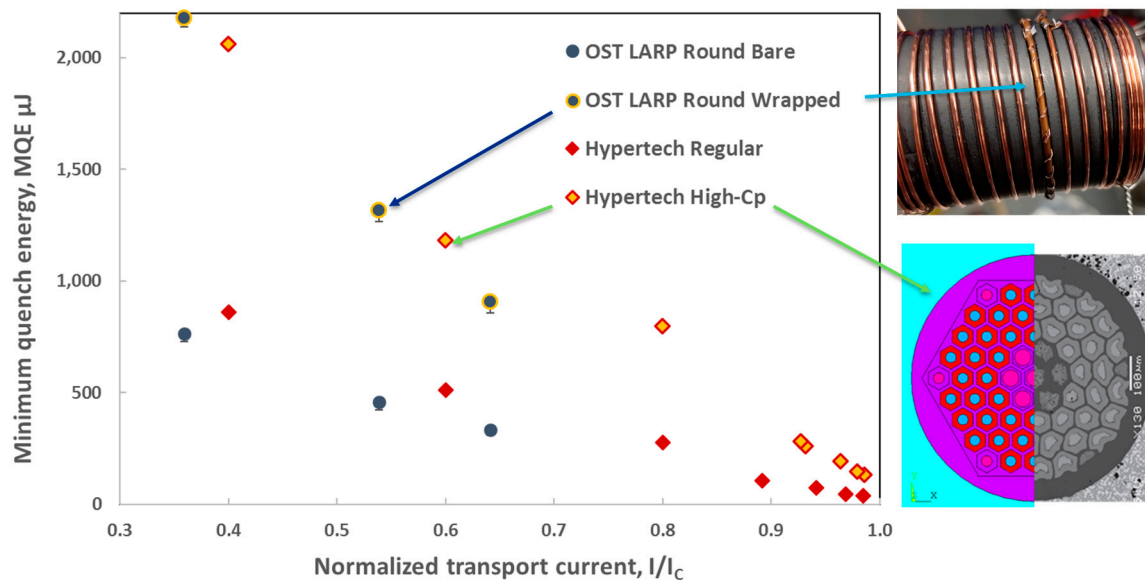


Figure 8. Comparison of MQE between high- C_p material in tape form and with high- C_p subelements within the strand geometry.

6. Conclusions

Several two-dimensional FEM thermal models were developed to study the MQE of Nb₃Sn composite superconducting wires. The developed thermal model was verified with experimental data. It was found that the position of the high-specific heat subelements has a negligible effect on the thermal efficiency of the wire. The quantity of high-specific heat subelements, i.e., the fraction of cross-sectional area occupied by these subelements, is more important against thermal perturbation. This result offers greater freedom for the development of new high- C_p composite wires and their mechanical feasibility.

Author Contributions: Data curation, F.B. and D.T.; Formal analysis, E.B. and D.T.; Investigation, F.B.; Methodology, E.B. and A.V.Z.; Software, F.B.; Validation, D.T.; Writing—original draft, E.B.; Writing—review & editing, A.V.Z. All authors have read and agreed to the published version of the manuscript.

Funding: This work was supported in part by Fermi Research Alliance, LLC, under Contract No. DE-AC02-07CH11359 with the U.S. Department and by the U.S.-Magnet Development Program.

Acknowledgments: The authors thank the U.S. MDP collaboration and the Fermilab Summer School of the University of Pisa.

Conflicts of Interest: The authors declare no conflict of interest.

References

1. U.S. Department of Energy, Office of Science. *The U.S. Magnet Development Program Plan*; Lawrence Berkeley National Lab. (LBNL): Berkeley, CA, USA, 2016.
2. Schoerling, D.; Zlobin, A.V. *Nb₃Sn Accelerator Magnets—Designs, Technologies, and Performance*; Schoerling, D., Zlobin, A.V., Eds.; Springer: Berlin, Germany, 2019; ISBN 978-3-030-16117-0.

3. Todesco, E.; Annarella, M.; Ambrosio, G.; Apollinari, G.; Ballarino, A.; Bajas, H.; Bajko, M.; Bordini, B.; Bossert, R.; Bottura, L.; et al. Progress on HL-LHC Nb₃Sn Magnets. *IEEE Trans. Appl. Supercond.* **2018**, *28*, 1–9. [[CrossRef](#)]
4. Kesgin, I.; Kasa, M.; Hasse, Q.; Ivanyushenkov, Y.; Shiroyanagi, Y.; Fuerst, J.; Barzi, E.; Turrioni, D.; Zlobin, A.V.; Gluskin, E. Development of short-period Nb₃Sn superconducting planar undulator. *IEEE Trans. Appl. Supercond.* **2019**, *29*, 1–4. [[CrossRef](#)]
5. Zlobin, A.; Novitski, I.; Barzi, E.; Kashikhin, V.V.; Carmichael, J.; Caspi, S.; Chlachidze, G.; Krave, S.T.; Orozco, C.; Schoerling, D.; et al. Development and first test of the 15 T Nb₃Sn dipole demonstrator MDPCT1. *IEEE Trans. Appl. Supercond.* **2020**, *30*, 1–5. [[CrossRef](#)]
6. Stoynev, S.E.; Riemer, K.; Zlobin, A.; Ambrosio, G.; Ferracin, P.; Sabbi, G.; Wanderer, P. Analysis of Nb₃Sn accelerator magnet training. *IEEE Trans. Appl. Supercond.* **2019**, *29*, 1–6. [[CrossRef](#)]
7. Hancox, R. Enthalpy stabilized superconducting magnets. *IEEE Trans. Magn.* **1968**, *4*, 486–488. [[CrossRef](#)]
8. Alekseev, P.; Boev, A.; Keilin, V.; Kovalev, I.; Kruglov, S.; Lazukov, V.; Sadikov, I. Experimental evidence of considerable stability increase in superconducting windings with extremely high specific heat substances. *Cryogenics* **2004**, *44*, 763–766. [[CrossRef](#)]
9. Alekseev, P.; Boev, A.; Keilin, V.; Kovalev, I.; Kozub, S.; Kostrov, E.; Kruglov, S.; Lazukov, V.; Sadikov, I.; Shutova, D. Influence of high heat capacity substances doping on quench currents of fast ramped superconducting oval windings. *Cryogenics* **2006**, *46*, 252–255. [[CrossRef](#)]
10. Field, M.B.; Zhang, Y.; Miao, H.; Gerace, M.; Parrell, J.A. Optimizing conductors for high field applications. *IEEE Trans. Appl. Supercond.* **2014**, *24*, 6001105. [[CrossRef](#)]
11. Peng, X.; Gregory, E.; Tomsic, M.; Sumption, M.D.; Ghosh, A.; Lu, X.F.; Cheggour, N.; Stauffer, T.C.; Goodrich, L.F.; Splett, J.D. Strain and magnetization properties of high subelement count tube-type Nb₃Sn strands. *IEEE Trans. Appl. Supercond.* **2011**, *21*, 2559–2562. [[CrossRef](#)]
12. Barzi, E.; Zlobin, A. Research and development of wires and cables for high-field accelerator magnets. *IEEE Trans. Nucl. Sci.* **2016**, *63*, 783–803. [[CrossRef](#)]
13. Xu, X.; Li, P.; Zlobin, A.V.; Peng, X. Improvement of stability of Nb₃Sn superconductors by introducing high specific heat substances. *Supercond. Sci. Technol.* **2018**, *31*, 03LT02. [[CrossRef](#)]
14. Hill, R.W.; Cosier, J.; Hukin, D.A. The specific heats of LaAg, GdAg and Gd₂O₃ from 0.5 to 22K. *J. Phys. C Solid State Phys.* **1983**, *16*, 2871. [[CrossRef](#)]
15. Xu, X.; Zlobin, A.; Peng, X.; Li, P. Development and study of Nb₃Sn wires with high specific heat. *IEEE Trans. Appl. Supercond.* **2019**, *29*, 1–4. [[CrossRef](#)]
16. Bonura, M.; Senatore, C. Thermal conductivity of industrial Nb₃Sn wires fabricated by various techniques. *IEEE Trans. Appl. Supercond.* **2013**, *23*, 6000404. [[CrossRef](#)]
17. Xu, X.; Zlobin, A.V.; Barzi-Fermilab, E.; Buehler, C.; Field, M.; Sailer, M.; Wanior, H.; Miao-Bruker, E.S.T.; Tarantini, C. Enhancing specific heat of Nb₃Sn conductors to improve stability and reduce training. In Proceedings of the CEC-ICMC 2019, Hartford, CT, USA, 21–25 July 2019.
18. Manfreda, G.; Barbagallo, C. *Review of ROXIE's Material Properties Database for Quench Simulation*. CERN, Magnets, Superconductors and Cryostats TE-MS. Internal Note 2018-1178007. Available online: file:///C:/Users/MDPI/AppData/Local/Temp/Materials_Manfreda.pdf (accessed on 16 September 2020).
19. Simon, N.J.; Drexler, E.S.; Reed, R.P. *Properties of Copper and Copper Alloys at Cryogenic Temperatures*; National Inst. of Standards and Technology (NIST), Boulder, CO (United States): New York, NY, USA, 1992.
20. Rondeaux, F.; Brédy, P.; Rey, J.M. Thermal conductivity measurements of epoxy systems at low temperature. In Proceedings of the Cryogenic Engineering Conference (CEC), Madison, WI, USA, 16–20 July 2001.
21. Swenson, C.A. Linear thermal expansivity (1.5–300 K) and heat capacity (1.2–90 K) of Stycast 2850FT. *Rev. Sci. Instrum.* **1997**, *68*, 1312–1315. [[CrossRef](#)]
22. Dargis, R.; Williams, D.; Smith, R.; Arkun, E.; Roucka, R.; Clark, A.; Lebby, M. Structural and thermal properties of single crystalline epitaxial Gd₂O₃ and Er₂O₃ grown on Si(111). *ECS J. Solid State Sci. Technol.* **2012**, *1*, N24–N28. [[CrossRef](#)]
23. Devred, A. *Quench Origins*; KEK Report 89–25, March 1990; National Laboratory for High Energy Physic: Tsukuba-shi, Japan, 1990.

24. Thompson, M.K.; Thompson, J.M. *ANSYS Mechanical APDL for Finite Element Analysis*, 1st ed.; Butterworth-Heinemann: Oxford, UK, 2017.
25. Summers, T.; Guinan, M.W.; Miller, J.R.; Hahn, P.A. A model for the prediction of Nb/sub 3/Sn critical current as a function of field, temperature, strain, and radiation damage. *IEEE Trans. Mag.* **1991**, *27*, 2041–2044. [[CrossRef](#)]



© 2020 by the authors. Licensee MDPI, Basel, Switzerland. This article is an open access article distributed under the terms and conditions of the Creative Commons Attribution (CC BY) license (<http://creativecommons.org/licenses/by/4.0/>).